Supporting Information:

An *In Situ* and Real Time Plasmonic Approach of Seed/Adhesion Layers: Chromium Buffer Effect at the Zinc/Alumina Interface

Maya Messaykeh,[†] Stéphane Chenot,[†] Pascal David,[†] Gregory Cabailh,[†] Jacques Jupille,[†] Alexey Koltsov,[‡] and Rémi Lazzari*,[†]

[†]*CNRS, Sorbonne Université, Institut des NanoSciences de Paris, UMR 7588, 4 Place Jussieu, F-75005 Paris, France*

[‡]*ArcelorMittal Maizières Research, voie Romaine, F-57280, Maizières-lès-Metz, France*

E-mail: remi.lazzari@insp.jussieu.fr

SI Photoemission quantification

Table SI: Binding energy (E_B), kinetic energy (E_K), transmission function (T_f) and photoionization cross-section (PICS)[1] of indicated core levels for Mg-Kα and Al-Kα excitations. $T_f \propto 1/E_K^{0.94}$ was estimated with the method of Cross and Castle.[2,3] E_B is not corrected from charge effects.

Core level	Al 2s		O 1s		Cr 2p		Zn 2p	
E_B(eV)	125		536		578.6		1026.7	
X-ray source	Mg	Al	Mg	Al	Mg	Al	Mg	Al
E_K(eV)	1128.6	1361.6	717.6	950.6	675	908	226.9	459.9
TF (arb. units)	1.35	1.13	2.07	1.59	2.19	1.67	6.10	3.14
PICS (arb. units)	1.15	0.77	4.84	3.07	19.53	12.12	46.57	30.03

Table SII: Effective attenuation lengths in Å (EAL) of indicated core levels for Mg-Kα and Al-Kα excitations in bulk Al_2O_3, Cr, Zn and Cr_2O_3. EALs are obtained by combining the elastic transport theory[4–6] and the TPP2M predictive formula[7] for inelastic mean free paths as implemented in the *I4P* package.[8]

Material	Al_2O_3		Cr		Zn		Cr_2O_3	
Density(mol.cm^{-3})	0.039		0.137		0.109		0.034	
X-ray source	Mg	Al	Mg	Al	Mg	Al	Mg	Al
Al 2s	27.2	31.5	17.8	20.6	17.8	20.7	21.6	24.9
O 1s	19.4	23.9	12.5	15.5	12.6	15.6	15.3	18.9
Cr 2p	–	–	11.9	15.0	12.0	15.0	14.7	18.2
Zn 2p	–	–	–	–	5.9	9.1	–	–

SII Surface Differential Reflectivity Spectroscopy (SDRS)

Surface Differential Reflectivity spectra of $Cr/Al_2O_3(0001)$ films have been fitted in the framework of the surface susceptibility formalism. By assuming a shape of truncated sphere or spheroid, the central issue is to evaluate the polarizabilities of a supported particle in the quasi-static approximation using a direct/image multipolar expansion of the electrostatic potential. Details about this dielectric modeling can be found in References 9–11. Calculations were performed at multipolar order $M = 24$ for particles arranged on an hexagonal lattice of parameter L with bulk dielectric functions[12] (Figure S1-a for Cr; $\epsilon = 3$ for alumina in the UV-visible range). During fits of experimental spectra, interparticle electrostatic interactions were accounted for at quadrupolar order.[9] As interband transitions in Cr may broaden resonances compared to the well-known metals of plasmonics (Ag, Au), simulations were first made to highlight the actual sensitivity of measurements to morphology. Figure S1-b,c shows a series of theoretical spectra for different aspect ratios $A_r = D_{\|}/h$ (in-plane diameter/height). Films of constant thickness (1.5 nm) made of truncated oblate hemispheroids for $A_r > 2$ and of truncated spheres for $A_r < 2$ are compared to the case of a continuous film. 3D (Volmer-Weber) and 2D (Frank-van-der-Merwe) growth modes have quite distinct optical signatures. By shifting from above 4 eV for poorly wetting situations down to 2.5 eV upon flattening, the broad resonance found in the UV-visible range is quite sensitive to as-

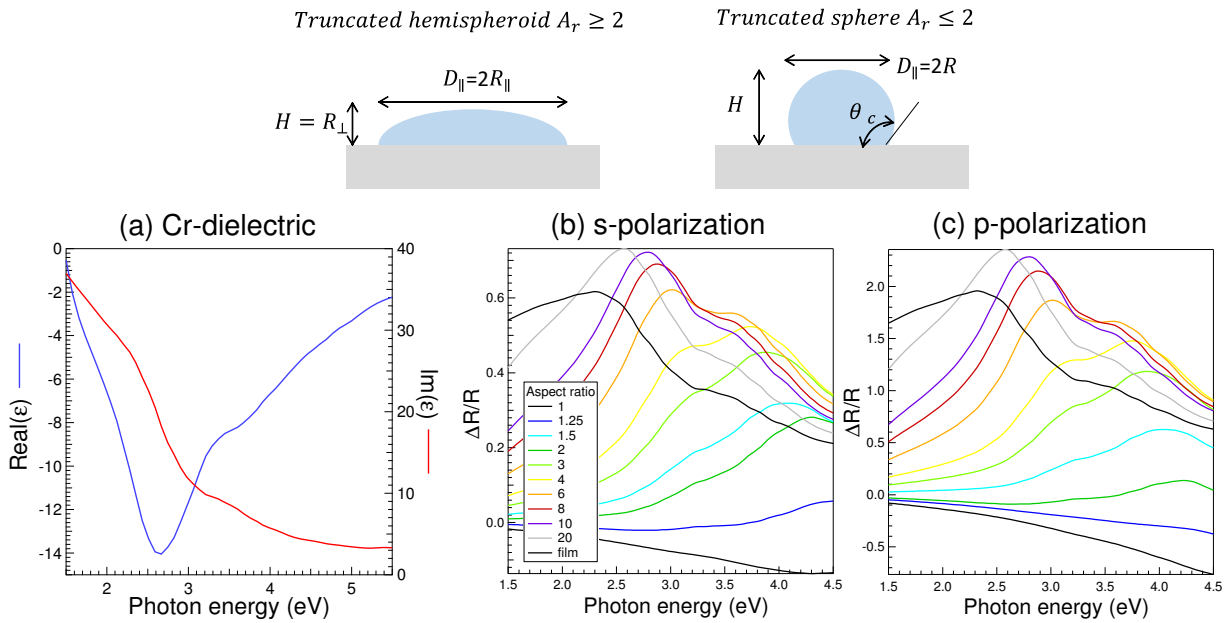

Figure S1: (a) Tabulated Cr dielectric function.[12] (b)(c) Simulated SDRS spectra for Cr/alumina particles of different aspect ratios in (b) s- and (c) p-polarization at an incident angle of $\theta_0 = 45°$. Particles are modeled by hemispheroids or truncated spheres (top scheme). The coverage was changed to keep the film thickness constant at 1.5 nm. No electrostatic interaction is accounted for between particles.

pect ratio. However measurements are poorly polarization dependent (Figure S1-b,c) since the resonance is dominated by a dipolar parallel mode as for Zn paricles.[13,14] However, combined with the inherent polydispersity broadening, a much lower sensitivity to inter-particle interaction is to be expected as shown by the simulations of Figure S2 performed already at a sizable surface coverage (45 %).

To analyze experimental data, χ^2-minimization was performed with constant error bars (0.005) on s-polarization spectra with the *GranFilm* software.[15,16] To cover a wide range of aspect ratios and therefore of spreading situations, a truncated oblate spheroidal shape was used herein.[11] But to limit the number of fitted parameters, only parallel radius $R_\parallel$, perpendicular radius $R_\perp$ and interparticle spacing L were fitted while keeping an hemispheroidal shape (see Figure S1-top). An *ad hoc* broadening of $\sigma_\parallel \sim 1$ eV had to be introduced by convolution (see Reference 17 for explanations) to obtain the agreement shown in the arti-

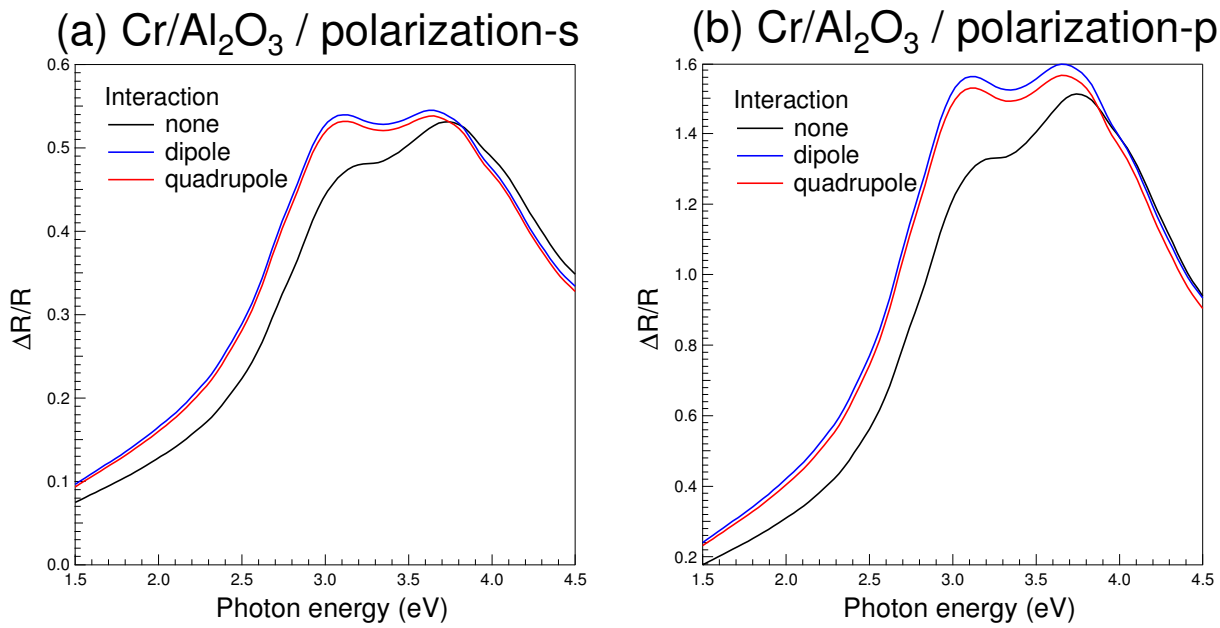

Figure S2: Effect of particle-particle interactions on simulated differential reflectivity spectra of Cr nanoparticles on alumina. Particles are modeled by hemispheroids of $R_{\parallel} = 10$ nm, $A_r = 4$ covering $\Theta = 45$ % of the substrate. Interaction are calculated on an hexagonal lattice of parameter $L = 28$ nm. The film thickness is $t = 1.5$ nm.

cle. Unfortunately, it turned out that the error bars of the fitted parameters ($a_1 = R_{\parallel}, a_2 = R_{\perp}, a_3 = L$) were important due to correlations close to 100 % as seen in the covariance matrix $V_{ij}^a = [C_{ij}^a]^{-1}$ which is the inverse of the curvature matrix at minimum χ^2: $C_{ij}^a = \frac{\partial \chi^2}{\partial a_i a_j}$. In other words, sizes and particle spacing are individually ill-defined. Since fitting in the *GranFilm* software is technically limited to those parameters, C_{ij}^a was transformed into a more physical set of parameters ($b_1 = t \propto R_{\parallel}^2 R_{\perp}/L^2, b_2 = A_r \propto R_{\parallel}/R_{\perp}, b_3 = \Theta \propto R_{\parallel}^2/L^2$), namely thickness t, aspect ratio A_r and surface coverage Θ . Their choice relies on the well-known intrinsic sensitivity of SDRS to the amount of matter (film thickness t) and the particle flattening (aspect ratio A_r).[17–19] Using the obvious relations between their logarithmic differential:

$$\begin{pmatrix} \frac{\delta t}{t} \\ \frac{\delta A_r}{A_r} \\ \frac{\delta \Theta}{\Theta} \end{pmatrix} = \begin{bmatrix} 1 & 1 & -2 \\ 1 & -1 & 0 \\ 2 & 0 & -2 \end{bmatrix} \begin{pmatrix} \frac{\delta R_{\parallel}}{R_{\parallel}} \\ \frac{\delta R_{\perp}}{R_{\perp}} \\ \frac{\delta L}{L} \end{pmatrix} ; \begin{pmatrix} \frac{\delta R_{\parallel}}{R_{\parallel}} \\ \frac{\delta R_{\perp}}{R_{\perp}} \\ \frac{\delta L}{L} \end{pmatrix} = \begin{bmatrix} 1 & 1 & -1 \\ 1 & 0 & -1 \\ 1 & 1 & -\frac{3}{2} \end{bmatrix} \begin{pmatrix} \frac{\delta t}{t} \\ \frac{\delta A_r}{A_r} \\ \frac{\delta \Theta}{\Theta} \end{pmatrix}, \qquad \text{(S1)}$$

and the transformation between curvature matrices:

$$C^b_{kl} = \sum_{i,j} \frac{\partial a_i}{\partial b_k} \frac{\partial \chi^2}{\partial a_i a_j} \frac{\partial a_j}{\partial b_l}, \tag{S2}$$

the new covariance matrix $V^b_{kl} = [C^b_{ij}]^{-1} = \left[\frac{\partial \chi^2}{\partial b_k b_l}\right]^{-1}$ was straightforwardly derived. As expected on the physics point of view, C^b_{kl} yielded much lower correlation coefficients except between Θ and t (not shown). The fitted parameters and the associated error bars as defined by the square-root of the diagonal elements of the covariance matrix are presented in article.

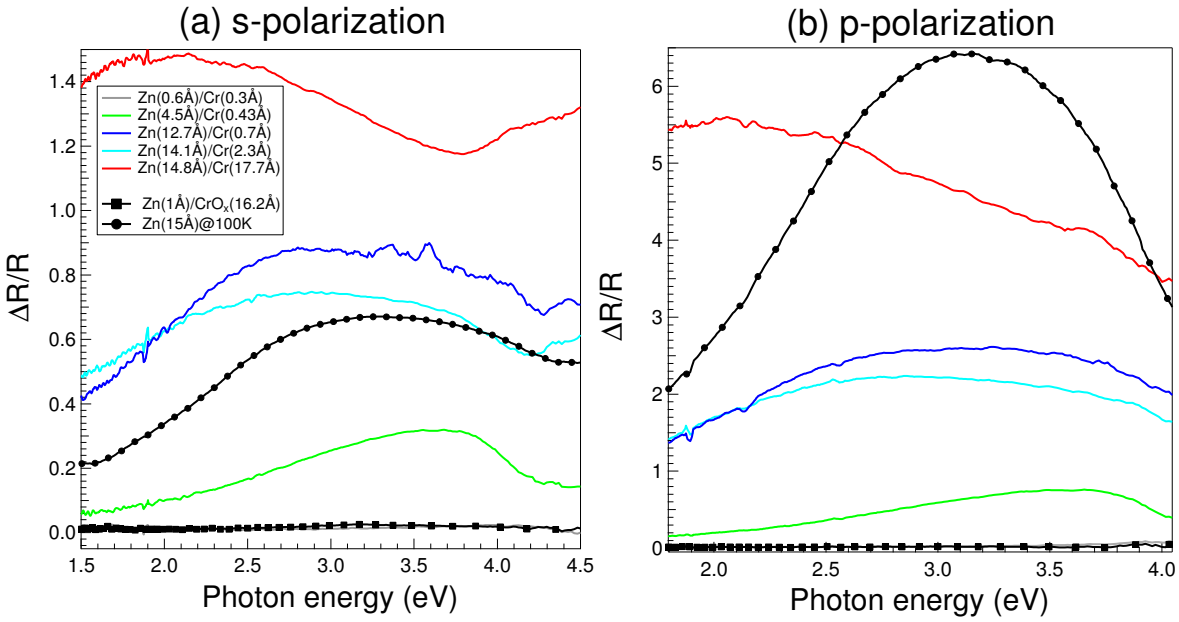

Figure S3: Differential reflectivity spectra of Zn/Cr/Al_2O_3(0001) in (a) s- and (b) p-polarization recorded after the exposure of Cr-precovered substrates to a constant dose of Zn ($\sim$ 15 Å) at 300 K. Thicknesses as calibrated by photoemission are given on the figure. All spectra are referenced to the bare alumina. A comparison is made to low temperature (100 K) growth of Zn on bare Al_2O_3.[20] Notice the enhancement of the intensity in p-polarization due to a lower reflection coefficient of alumina. The difference of intensity at about the same thickness for the 100 K deposit is due to a different incident angle (55° instead of 45° for all other spectra) closer to the Brewster angle of the alumina substrate.

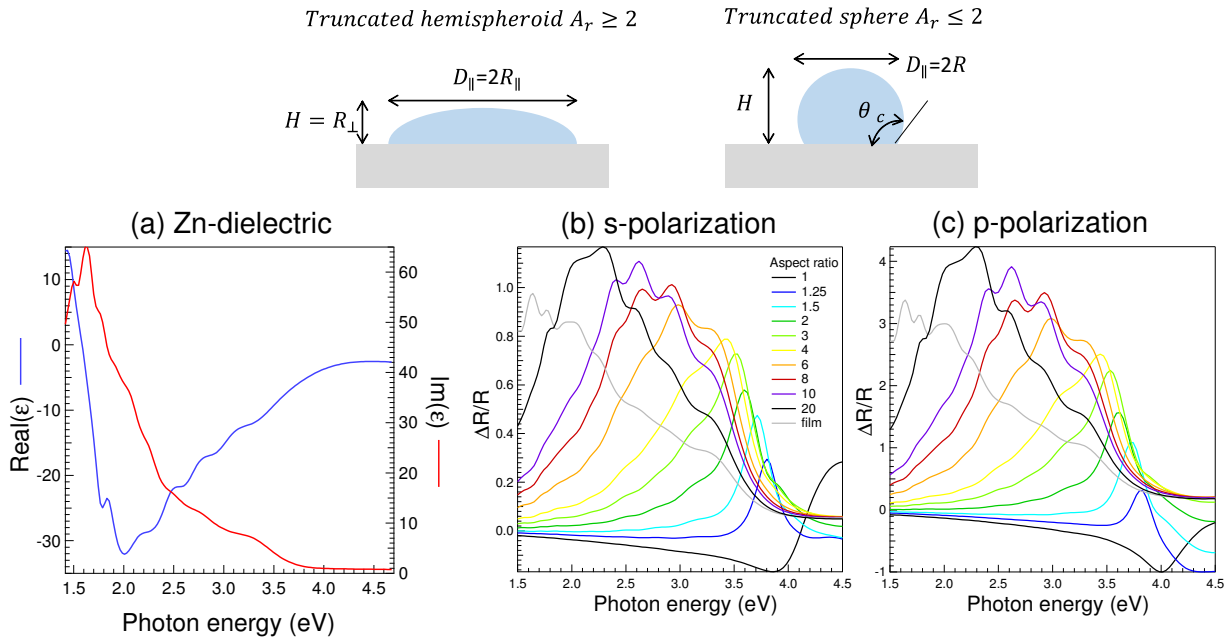

Figure S4: Same figure as Figure S1 but for Zn/Al_2O_3. The dielectric function of Zn can be found in Reference 21.

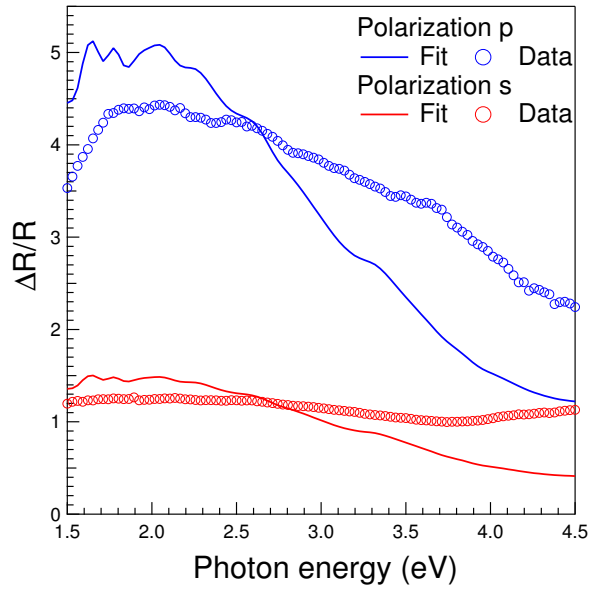

Figure S5: Comparison between SDRS simulations (lines) of a stack of two continuous films Zn(14.8 Å)/Cr(17.7 Å)/Al_2O_3(0001) and the corresponding experimental spectra (symbols). Polarization state is indicated on the figure.

SIII Temperature Programmed Desorption (TPD)

Prior to line shape analysis of TPD, a background similar to the Shirley one commonly used in photoemission[22] was subtracted to compensate for the slight increase in residual pressure in the quartz tube and to zero the tails of spectra at temperatures T_1 (before the peak) and T_2 (after the peak) (see figure S6-a). In other words, the background signal $s_b(T)$ is assumed to be proportional to the integral of the desorption signal $s_d(T)$ up to a given temperature T:

$$s_b(T) = s_d(T_1) + [s_d(T_2) - s_d(T_1)] \frac{\int_{T_1}^{T} s_d(T')dT'}{\int_{T_1}^{T_2} s_d(T')dT'}. \tag{S3}$$

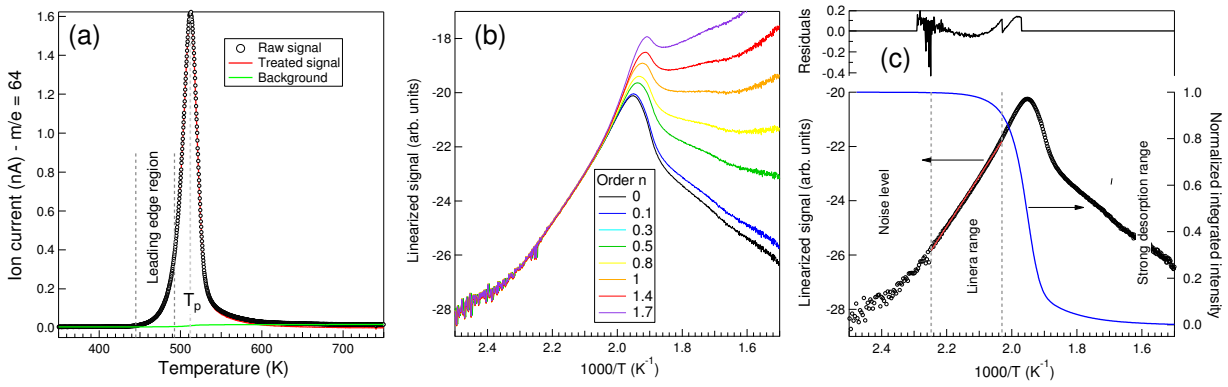

Figure S6: Example of TPD spectrum analysis for a Zn(0.5 Å)/Cr(0.8 Å)/Al_2O_3(0001)-(1×1) deposit: (a) Raw (circles) and background subtracted $s_d(T)$ (red line) signals for $m/e = 64$ are compared (see text). Vertical dotted lines show the leading edge region and the peak position T_p used in the quantitative analysis. (b) Linearized desorption spectra $\mathcal{S}_d(n,T) = \ln[s_d(T)] - n \ln\left[\int_T^\infty s_d(T')dT'\right]$ for desorption orders n indicated in the inset (see Reference 20). (c) Linear fit (red line) of $\mathcal{S}_d(0,T)$ in the leading edge region in an Arrhenius graph (left scale). The evolution of the integrated signal is plotted on the right scale (blue line) showing that the amount of Zn on the surface is nearly constant in the analyzed range of temperature. The spectrum corresponds to that of Figure-a where the fit region is indicated by dotted lines.

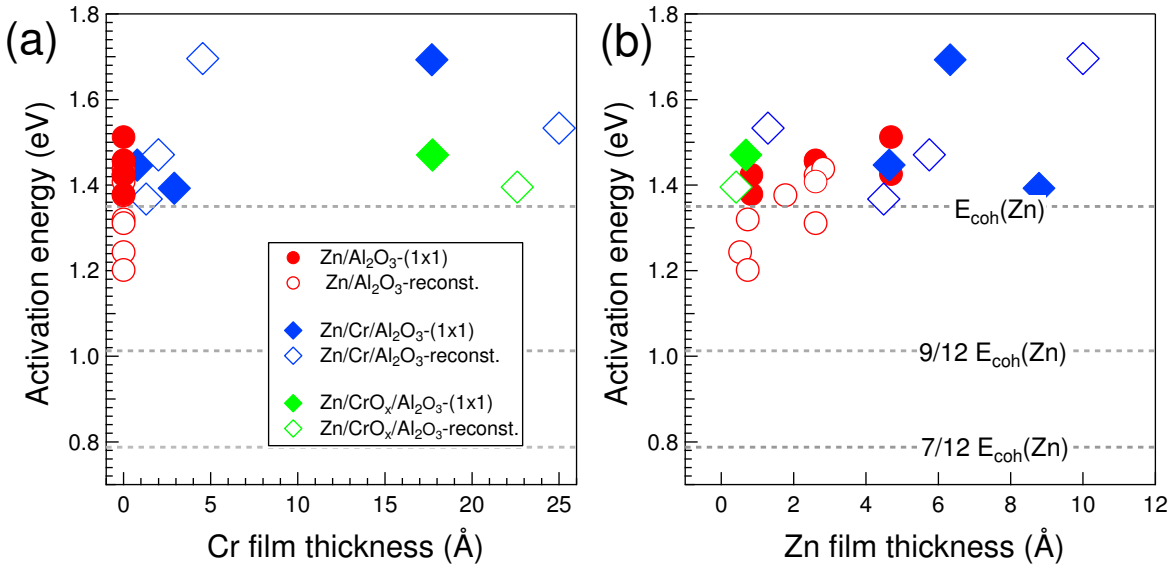

Figure S7: Activation energy of Zn desorption deduced from the Redhead analysis as a function of (a) Cr and (b) Zn film thicknesses for (1×1) and reconstructed surfaces. Data are compared to the bare surface case[20,23] (red points) and the cohesive energy of zinc (dotted lines; see text). The Redhead approach overestimates the desorption energies.

References

(1) Yeh, J.; Lindau, I. Atomic subshell photoionization cross sections and assymetry parameters: $1 \leq Z \leq 300$. *At. Data Nucl. Data Tables* **1985**, *32*, 1–155.

(2) Cross, Y. M.; Castle, J. E. The relationship between transmission efficiencies in the FRR and FAT modes of an electron spectrometer. *J. Electron Spectrosc. Relat. Phenom.* **1981**, *22*, 53 – 60.

(3) Ruffieux, P.; Schwaller, P.; Gröning, O.; Schlapbach, L.; Gröning, P.; Herd, Q. C.; Funnemann, D.; Westermann, J. Experimental determination of the transmission factor for the Omicron EA125 electron analyzer. *Rev. Sci. Instr.* **2000**, *71*, 3634–3639.

(4) Jablonski, A.; Powell, C. J. The electron attenuation length revisited. *Surf. Sci. Rep.* **2002**, *47*, 33–91.

(5) Jablonski, A.; Powell, C. J. Improved algorithm for calculating transport cross sections of electrons with energies from 50 eV to 30 keV. *Phys. Rev. B* **2007**, *76*, 085123.

(6) Jablonski, A. Photoelectron transport in the surface region of solids: universal analytical formalism for quantitative applications of electron spectroscopies. *J. Phys. D: Appl. Phys.* **2015**, *48*, 075301.

(7) Tanuma, S.; Powell, C. J.; Penn, D. R. Calculation of electron inelastic mean free paths (IMFPs) VII. Reliability of the TPP-2M IMFP predictive equation. *Surf. Interface Anal.* **2003**, *35*, 268–275.

(8) Lazzari, R. `Igor Pro Paris Photoemission Package` can be downloaded with a user guide from: http://www.insp.upmc.fr/I4P-Igor-Pro-Paris-Photoemission.html?lang=en.

(9) Bedeaux, D.; Vlieger, J. *Optical Properties of Surfaces*; Imperial College Press: London, 2001.

(10) Simonsen, I.; Lazzari, R.; Jupille, J.; Roux, S. Numerical modelling of the optical response of supported metallic particles. *Phys. Rev. B* **2000**, *61*, 7722–7733.

(11) Lazzari, R.; Simonsen, I.; Bedeaux, D.; Vlieger, J.; Jupille, J. Polarizability of truncated spheroidal island supported by a substrate : models and applications. *Eur. Phys. J. B* **2001**, *24*, 267–284.

(12) Palik, E. D. *Handbook of Optical Constants of Solids*; Academic Press, 1985; Vol. 1-3.

(13) Lazzari, R.; Jupille, J.; Cavallotti, R.; Simonsen, I. Model-free unraveling of supported nanoparticles plasmon resonance modes. *J. Phys. Chem. C* **2014**, *118*, 7032–7048.

(14) Messaykeh, M. A fundamental approach of the wetting at $Zn/Cr/Al_2O_3$ interface: the effect of a Cr buffer. Ph.D. thesis, Sorbonne University, France, 2018.

(15) Lazzari, R.; Simonsen, I. `GranFilm`: a software for calculating thin-layer dielectric properties and Fresnel coefficients. *Thin Solid Films* **2002**, *419*, 124–136.

(16) `GranFilm` can be downloaded with a user guide from: http://www.insp.jussieu.fr/-Logiciels-.html.

(17) Lazzari, R.; Jupille, J. Quantitative analysis of nanoparticle growth through plasmonics. *Nanotechnology* **2011**, *22*, 445703.

(18) Lazzari, R.; Simonsen, I.; Jupille, J. Interfacial susceptibilities in nanoplasmonics via inversion of Fresnel coefficients. *Plasmonics* **2014**, *9*, 261–272.

(19) Lazzari, R.; Jupille, J.; Cavallotti, R.; Chernysheva, E.; Castilla, S.; Messaykeh, M.; Hérault, Q.; Meriggio, E. Plasmonics of supported nanoparticles reveals adhesion at the nanoscale: implications for metals on dielectrics. *ACS Applied Nano Materials* **2020**, *3*, 12157–12168.

(20) Thi Le, H.-L.; Lazzari, R.; Goniakowski, J.; Cavallotti, R.; Chenot, S.; Noguera, C.; Jupille, J.; Koltsov, A.; Mataigne, J.-M. Tuning adhesion at metal/oxide interfaces by surface hydroxylation. *J. Phys. Chem. C* **2017**, *121*, 11464–11471.

(21) Nash, D. J.; Sambles, J. R. Surface plasmon-polariton study of the optical dielectric function of zinc. *J. Mod. Opt.* **1998**, *45*, 2585–2596.

(22) Shirley, D. High-resolution X-ray photoemission spectrum of valence bands of gold. *Phys. Rev. B* **1972**, *5*, 4709–4714.

(23) Cavallotti, R. Effets de la terminaison de l'α-alumine sur le comportement au mouillage du zinc. Ph.D. thesis, Pierre and Marie Curie University, France, 2014.